

# Imaging atomic scattering potential in centroidal diffraction of elastic electrons

R. Aiswarya,<sup>1</sup> Jobin Jose,<sup>1,\*</sup> Nenad Simonović,<sup>2</sup> Bratislav P. Marinković,<sup>2,†</sup> and Himadri S. Chakraborty<sup>3,‡</sup>

<sup>1</sup>*Department of Physics, Indian Institute of Technology Patna, Bihar 801103, India*

<sup>2</sup>*Institute of Physics Belgrade, Pregrevica 118, Belgrade, Serbia*

<sup>3</sup>*School of Natural Sciences, D.L. Hubbard Center for Innovation, Northwest Missouri State University, Maryville, Missouri 64468, USA*

The Fraunhofer diffraction of quantum particles from materials with sharp electron-density edges or symmetric bond structures is ubiquitous. In contrast, diffraction from atoms with characteristic asymptotically-diffused electron distribution is far less intuitive, although known for many years. The current study unravels an unusual diffraction mechanism of elastic electrons from diffused atomic diffractors. Consequently, the fringe pattern converted to the Fourier reciprocal space maps out the effective scattering potential, which is *not* accessible in direct measurements. This may benefit benchmarking theory models, advances in atom-holography, plasma and astrophysical diagnostics, and accessing time-resolved potential landscapes. The study employs relativistic partial wave analysis with atoms modeled in the Dirac-Fock formalism and performs *e*-Cd measurements in absolute scale. Analysis for Mg, Ba, and Ra targets demonstrates the universality of the mechanism.

Varieties of structural information of matter are eminently extractable by diffracting charged particles (electrons or positrons) off materials. For systems more complex than atoms, it is straightforward to understand the bending of projectile plane wave into spherical waves from the well-defined edges of the delocalized electron-cloud and from the localized atomic or lattice centers. This results in the overlap of spherical waves with specific path-differences leading to diffraction features whose Fourier transform (FT) can reveal real-space structural information. For electron projectiles, capturing the scattering signal by a charge-coupled-device detector and the transmission signal by a transmission electron microscope are at the center of Fraunhofer-type diffraction studies. Examples include studies of molecules [1–4], nanostructures [5], surfaces [6], and crystals [7]. Recently, the *e*-C<sub>60</sub> scattering study [8] has shown that diffraction effects can be captured in two modes, (i) in the scattering angular distribution with a fixed impact energy (*E*) or momentum and (ii) in the impact energy distribution at a fixed scattering direction, with possible benefits in ultrafast electron diffraction research.

The first experimental evidence of diffraction in scattering by simple gas-phase atoms was detected a century ago by Dymond [9] and Bullard & Massey [10]. Today, crossed-beam electron scattering has become increasingly multi-dimensional, combining kinematic coincidence detection [11], ultrafast time-resolution [12], control over target orientation/state [13], and extension to complex systems [14]. These advances are crucial for accessing electron correlation, scattering dynamics, and quantum many-body phenomena. Meanwhile, powerful methods, like partial wave analysis [15] and quantum defect theory [16], are formulated to describe low- and high-energy

collisions and resonances. Later, Dirac partial wave analysis included relativistic effects [17, 18]. Techniques, such as, close-coupling theory [19], R-matrix [20], relativistic distorted wave approximation [21], distorted-wave Born approximation [22], relativistic-coupled cluster [23, 24], and optical potential modeling using density functional theory [25] incorporated electron exchange and correlation effects. Thus, high-accurate *e*-atom scattering predictions were possible, including routinely prevalent diffraction structures matching measurements [26–38].

However, the electron diffraction from atoms is largely counterintuitive, since the localized orbital-density under long-range interaction monotonically fizzles away with the distance from the nucleus and thus does not produce a ready “edge”. In fact, no clear attempt has been made to interpret the *e*-atom diffraction, except simply assuming that the atom presents a “dark” disk [39]. We attempt to fill this gap in the current theory-experiment study. This new understanding ushers a valuable benefit: by transferring the diffraction pattern in the elastically scattered angular distribution to the Fourier conjugate space for various incident momenta it is possible to image the effective atomic scattering potential.

Diffraction is also commonplace in the photoionization (PI) of symmetric molecules [41] and clusters [42, 43]. Even though for the PI of a spherical system the angular distribution mode of diffraction is forbidden due to the symmetry, the diffraction is accessible in the photoelectron energy distribution. In distinction, for the scattering by even a spherical system, the presence of the projectile breaks the overall symmetry. In any case, a simpler way to understand the diffraction in PI is to consider the spatial gradient of the ground state potential that the photoelectron escapes. This gradient is stronger at the edge of a delocalized electron distribution and at the interatomic bond edges in molecules. Hence, local electron emissions occur from these regions due to the availability of strong ionizing force (potential gradient), the key quantity within the acceleration gauge formalism of PI. Consequently, diffraction results. In contrast, for a sin-

\* [jobin.jose@iitp.ac.in](mailto:jobin.jose@iitp.ac.in)

† [bratislav.marinkovic@ipb.ac.rs](mailto:bratislav.marinkovic@ipb.ac.rs)

‡ [himadri@nwmissouri.edu](mailto:himadri@nwmissouri.edu)

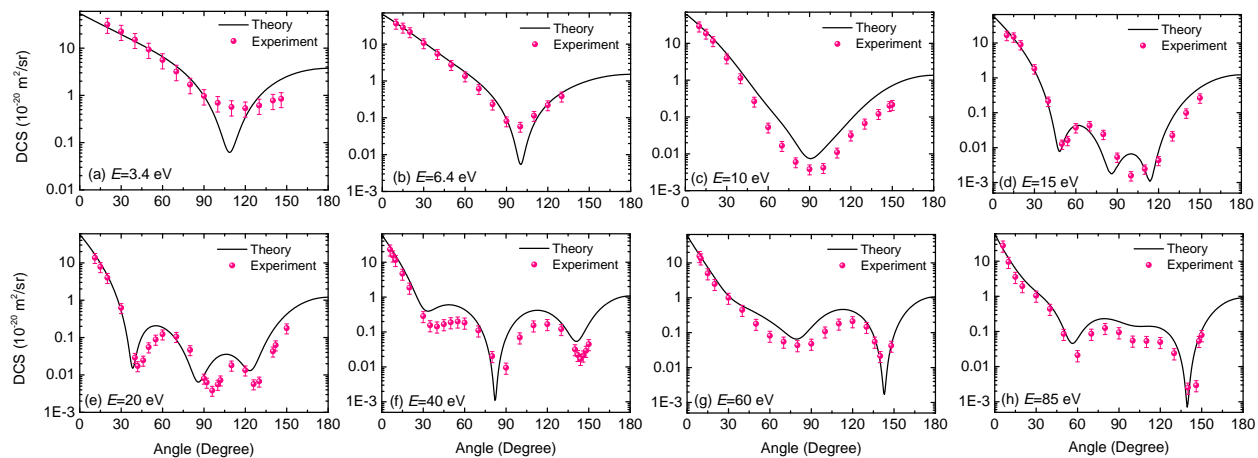


FIG. 1. Absolute angular DCS of  $e$ -Cd for collision energies 3.4 (a), 6.4 (b), 10 (c), 15 (d), 20 (e), 40 (f), 60 (g), and 85 (h) eV are compared for current measurement versus calculation. The TCS comparison in Fig. S2 is given in SM [40].

gle atom, Coulomb potential entirely forbids diffraction in PI, since  $\frac{d}{dr}(-\frac{Z}{r})$  being continuous suggests no cite-specific emission. So the fundamental question is: what is the leading process that underpins diffraction in scattering from atoms, which do not have density edges? To elucidate, we employ an interpretative model that reveals a centroidal diffraction mechanism. This effectuates average diffractor sizes as a function of  $E$  that map the net profile of the interaction potential.

Details of the theory are given in Supplementary Material (SM) [40]. The electron density of the atomic target is obtained using the self-consistent relativistic Dirac-Fock formalism [44]. The  $e$ -atom interaction potential is constructed in an optical model approach [25], which incorporates effects of exchange and correlation. Scattering parameters are computed within the relativistic partial wave framework. The scattering phase shifts,  $\delta_\kappa$ , are obtained by numerically solving the coupled radial Dirac equations with the interaction potential  $V_{\text{Opt}}$  [45] as

$$\begin{aligned} \frac{dP_{E\kappa}(r)}{dr} &= -\frac{\kappa}{r}P_{E\kappa}(r) + \frac{E - V_{\text{Opt}} + 2m_e c^2}{\hbar c}Q_{E\kappa}(r) \\ \frac{dQ_{E\kappa}(r)}{dr} &= -\frac{E - V_{\text{Opt}}}{\hbar c}P_{E\kappa}(r) + \frac{\kappa}{r}Q_{E\kappa}(r), \end{aligned} \quad (2)$$

where  $P_{E\kappa}(r)$  and  $Q_{E\kappa}(r)$  represent the large and small component of the radial wave function, respectively; see the meaning of other terms in SM [40]. Using  $\delta_\kappa$ , the scattering amplitudes are calculated, from which the differential cross section (DCS) is obtained as [17]:

$$\frac{d\sigma}{d\Omega} = |f(k, \theta)|^2 + |g(k, \theta)|^2, \quad (3)$$

where  $f(k, \theta)$  and  $g(k, \theta)$  are direct and spin-flip amplitudes. Previous studies using Dirac partial wave analysis showed excellent agreement between calculated and experimental cross sections for atoms [51–54]. The DCS depends on the magnitude of incident momentum  $k =$

$\sqrt{2E}$ , in atomic units (a.u.), and scattering angle  $\theta$ . In elastic scattering, the magnitude of momentum transfer

$$q = 2k \sin(\theta/2). \quad (4)$$

Obviously, the variation in  $q$  can be affected by either scanning  $\theta$  with fixed  $E$  ( $k$ ) or tuning  $E$  while looking along a fixed  $\theta$ , laying out a 2D diffraction landscape [8].

Experimental data for  $e$ -Cd collision are collected using a crossed-beam spectrometer where a mono-energetic electron beam is focused onto the atomic beam, and the scattered electrons are detected as a function of  $E$  and  $\theta$ . The principal parts of the spectrometer are: (i) the vacuum chamber containing an oven for metals, an electron source with a monochromator and a scattered electron detector with an analyzer; (ii) the system of vacuum pumps and electric power supplies; and (iii) measuring instruments [55]. The oven heated by coaxial wires is used to produce a gas-phase atoms beam by vaporizing a solid sample [56]. The monochromator and analyzer were constructed as systems of cylindrical electrostatic lenses with hemispherical dispersion elements. The electron optics was designed along principles outlined by Kuyatt [57] and by Chutjian [58]. The  $E$  range of the impact electrons was from several eV to 100 eV with the resolution of the spectrometer of about 50 meV, and the scattering angles ranged from  $6^\circ$  to  $150^\circ$ .

In Figure 1, our measured angular DCS in the absolute scale (numerical data in SM [40]) of elastic  $e$ -Cd for a selection of  $E$  compares well with our calculations. Results show maxima and minima, in varied intensities, representing bright and dark diffraction fringes. Even though at lower  $E$  theory somewhat over-sharpens the minima, the qualitative agreement is obvious. Generally, this fringe pattern is seen to shrink with increasing  $E$ .

The  $\theta$  scan of the computed DCS for a given  $k$  can be converted to  $q$ -scale by Eq. (4). As characteristic of the diffraction, the FT of the pattern in  $q$  yields the diffraction length in the reciprocal (real) space that connects to

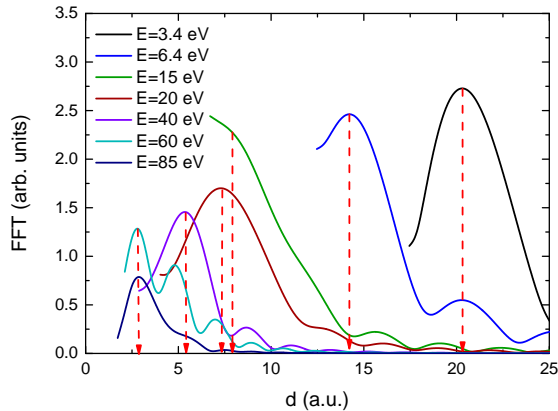


FIG. 2. FFT spectra of calculated DCS in Fig. 1 for all energies except 10 eV. Red arrows point the peak locations.

the size of the diffractor electrons experience. We carry out FT following Ref. [8]. To capture the pure diffraction component in DCS, we curve-fit the non-diffractive background [59] and subtract it from the full signal before applying a fast FT (FFT). Resulting FFT spectra, for the set of  $E$  in Fig. 1, are presented in Figure 2. These spectra emerge in two-times-radial scale  $d = 2r$  (see in the following). As noted, the FFT reveals distinct peaks for different  $E$ , except for 10 eV (due to weak diffraction signal both in theory and experiment) which we leave out. As evident, the peak location, at 20.2 a.u. for the lowest 3.4 eV, gradually decreases to 2.82 a.u. for the highest 85 eV. Thus, as  $E$  increases, the FFT peaks move closer to the nucleus, indicating that higher the electron energy the smaller the diffraction length it senses. So, the natural question is: What makes the progressively energetic electron to see smaller diffracting size?

Before we answer this question, let us illustrate by iso-surface images in Figure 3, the complete 2D diffractograms computationally simulated for a smaller Mg and a larger Cd. Both modes,  $\theta$ -scan at fixed  $k$  and  $k$ -scan at fixed  $\theta$ , are depicted in polar graphs of DCS.  $k$  is plotted along the radius, such that at a given radius going over a circle is the former mode, while at a given direction going along a radius is the latter. As expected, the maximum DCS is noted in the forward direction. More importantly, the overall structures being richer for Cd points a shrunk pattern for a larger target from the inverse relation of the diffraction length and inter-fringe separation.

We introduce a model pathology to understand the evolution of the FT-derived diffracting length as  $E$  ( $k$ ) tunes. Consider the elastic Born amplitude of in a.u.,

$$f_B(k, \theta) = 2 \int_0^\infty dr r^2 \frac{\sin(qr)}{qr} V(r). \quad (5)$$

Recalling Eq. (4), we may write

$$q \approx 2k - k \cot^2(\theta/2). \quad (6)$$

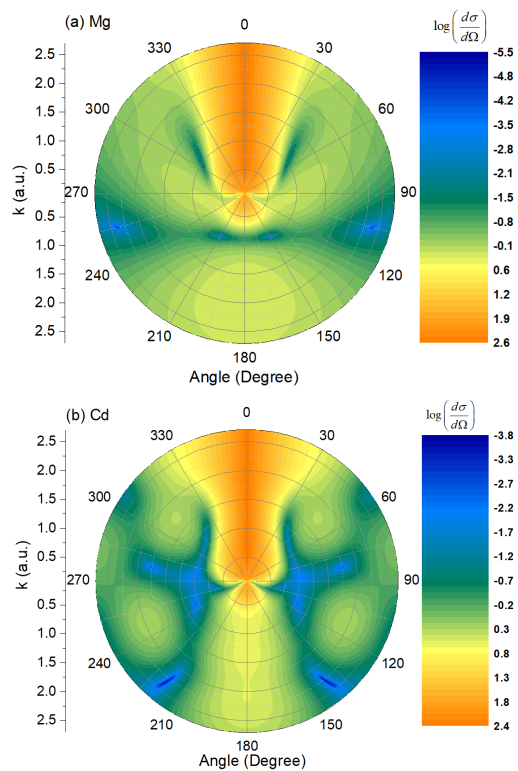


FIG. 3. Diffractograms calculated for (a)  $e$ -Mg and (b)  $e$ -Cd.

In approximating Eq. (6) we ignore the forward scattering, where  $\cot(\theta/2)$  is large, so we retain up to the linear power of  $\cot^2(\theta/2)$  in the Taylor expansion. This goes without any loss of generality, since no appreciable diffraction exists in the forward direction (Fig. 3). Plugging Eq. (6) in the relevant part of Eq. (5) one obtains,

$$f_B(k, \theta) \approx \frac{2}{q} \int_0^\infty dr r \sin[2kr - kr \cot^2(\theta/2)] V(r). \quad (7)$$

It is now helpful to split the Born amplitude between a non-diffractive steady background (bg) and a pure diffractive (df) component, and recognize that the dominant diffraction arises from  $r = b$ . Here,  $b = (L/k^2) \cot(\theta/2)$  is the classical impact parameter of collision with  $L = Z/(4\pi\epsilon_0)$ . This enables a further approximation of the diffraction amplitude as,

$$f_B^{(df)}(k, \theta) \approx \frac{2}{q} b(\theta) \sin[2kb(\theta)] V[b(\theta)], \quad (8)$$

in which, obviously,  $\theta$ -scan maps into the variation of  $b$ , with  $b$  decreasing towards the backward scattering.

For clarity, we invoke average  $b$  as  $b_c$  to write  $b = b_c + \alpha$ , where  $\alpha >$  and  $< 0$  define outer and inner locations of  $b$  from  $b_c$  directly varying with  $\theta$ . Hence, Eq. (8) reads as,

$$\begin{aligned} f_B^{(df)}(k, \theta) &\approx \sin[2k(b_c + \alpha)] \left( \frac{2}{q} (b_c + \alpha) V(b_c + \alpha) \right) \\ &= \sin[2kb_c + 2k\alpha] \mathcal{F}(\alpha), \end{aligned} \quad (9)$$

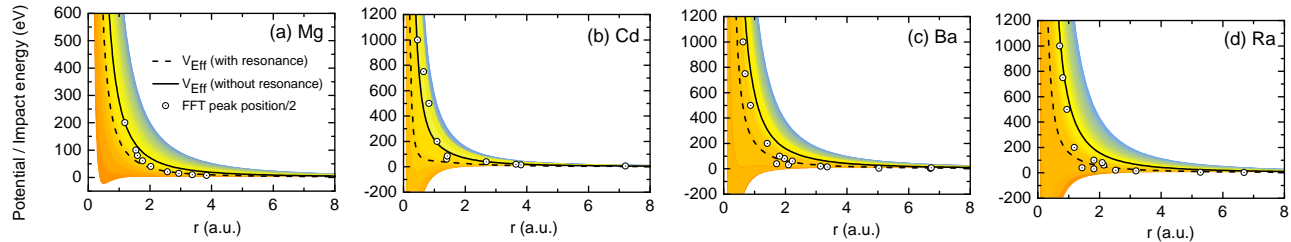


FIG. 4. Effective potential  $V_{\text{Eff}}$  [Eq. (12)] averaged over the range 0.1 - 100 eV using TCS with and without the resonance. Color bands image  $V(r, E)$  shapes across this range. FFT peak locations, divided by two, for different  $E$  are plotted by dots.

such that we express the full amplitude in the form:

$$f_B(k, \theta) \approx f_B^{(\text{bg})} + \sin(2kb_c + 2k\alpha)\mathcal{F}(\alpha). \quad (10)$$

Eq. (3), ignoring  $|\mathcal{F}|^2$ , yields the Born DCS as

$$\frac{d\sigma}{d\Omega_B} \sim \frac{d\sigma}{d\Omega_B}^{(\text{bg})} + 2 \sin[2kb_c + 2k\alpha] f_B^{(\text{bg})} \otimes \mathcal{F}(\alpha) \quad (11)$$

We argue, the interference term from quantum coherence containing  $\otimes$  above embodies a notion of diffraction.

Evidently in Eq. (11), the diffraction dominates with no dephasing as  $\alpha = 0$  or  $b = b_c$ . Here, the deBroglie wavelength of  $k$  will match  $2b_c$ , rendering  $2b_c$  to be the diffraction length. Including  $\alpha$ 's, however,  $2b_c$  modifies to a *centroid* location due to the averaging, weighted by  $f_B^{(\text{bg})} \otimes \mathcal{F}(\alpha)$  in Eq. (11) for individual Fourier components. Thus, the position of the FT peak provides a centroidal diffraction-size for a given  $k$  ( $E$ ). We show below, by varying  $E$  and applying FT to angular DCS we map out a profile that images the scattering potential.

Since the scattering potential is a function of  $E$ , we employ the weighted averaging (SM [40] for details)

$$V_{\text{Eff}}(r) = \frac{\sum_i V(r, E_i) \sqrt{\sigma(E_i)}}{\sum_i \sqrt{\sigma(E_i)}} \quad (12)$$

to determine the effective interaction potential the projectile explores. As the diffraction vanishes in total (angle-integrated) CS (TCS),  $\sigma$ , such that  $\sqrt{\sigma} \sim |f_B^{(\text{bg})}|$ , the weight factor in Eq. (12) is consistent with  $f_B^{(\text{bg})} \otimes \mathcal{F}(\alpha)$  in Eq. (11) for each Fourier component. Indeed, remarkably, the half of the FFT peak positions as  $E$  varies, like in Fig. 2, closely follow the  $V_{\text{Eff}}$  shape for Cd, panel (b), in Figure 4. We also include results to verify this prediction for Mg, Ba and Ra which reinforces the generality of the phenomenon, at least for closed shell atoms/ions. Note, for the smallest atom Mg, we do not find enough diffraction signal for FFT at  $E = 500, 750$  and  $1000$  eV. The potential bands for the  $E$  range 0.1-100 eV considered for averaging are shown as color-maps in Fig. 4.

We make two observations in Fig. 4. (i) The low- $E$  end of potential bands exhibits attractive (negative) shapes which becomes stronger with larger targets. These spawn resonances in TCS at low  $E$  from metastable binding

of slow projectiles (Fig. S1 in SM [40]). One effect of these resonances is the accumulation of some FFT data points for Cd, Ba and Ra that fall outside the trend lines. (ii) Assuming the resonances not participating in the potential imaging, we applied non-resonant  $\sigma$ 's in Eq. (12) to plot. However, we also plot the potential weighted with resonant  $\sigma$ 's. As seen, while the latter show better propensity to match with the FFT trend at lower  $E$ , the former succeeds at higher  $E$ . There is another implication of this result. The sharper resonances suggest longer lifetimes of slow electron's binding. Thus, for a diffraction study of scattering time delay [60], this longer delay trapped in resonance states may remain insensitive to fast scattering in imaging scattering potential [61].

Imaging the scattering potential through  $e$ -atom diffraction promises impacts in research and technology. Atomic-level potential mapping may enable experimental validation and refinement of quantum models / simulations for benchmarking, including insights into short-range forces, phase shifts, and even developing holographic atom-imaging [62]. The knowledge may aid the (i) design of catalysts [63] by revealing how atomic-scale potentials influence reaction pathways, (ii) modeling ionization / excitation / recombination in hot plasmas to diagnose fusion environments [64], and (iii) interpretation of spectral lines, emission profiles, and energy dissipation in planetary, stellar and interstellar media [65]. Not the least, in time-resolved electron diffraction the imaging of potential landscapes in time may offer new tools to access ultrafast resonances and coherence.

To conclude, this theory-experiment joint study presents and compares absolute-scale angularly-distributed DCS for  $e$ -Cd elastic scattering for a range of impact energies. While the diffraction patterns in  $e$ -atom scattering is known for a long time, the understanding of the mechanism was vastly elusive. We perform a fully quantum calculation but illustrate an approach to uncover a centroidal diffraction phenomenon intrinsic to scattering from edge-less, smudgy atomic boundaries, as opposed to the regular diffraction from semi-discrete boundary of molecular potentials and bonds. The approach demonstrates that the overall diffracting length, obtained from the FT of DCS fringes to the reciprocal space, as a function of energy can delineate the scattering potential – a cardinal collision

parameter not directly observable in experiments. Proving the universality of the result, the method is shown to be also successful for Mg, Ba, and Ra. This offers a spectroscopic route to capture a quantitative scattering force within the long-range atomic potential and opens a new route to explore atomic interactions at a fundamental level. The study may develop technology and research applications, and may infuse scopes in the field of ultrafast electron diffraction [66, 67].

## ACKNOWLEDGMENTS

The research is supported by: CRG/2022/000191, India (J.J.); Institute of Physics Belgrade, through a grant from the Ministry of Science, Technological Development and Innovation of the Republic of Serbia (N.S.); Science Fund of the Republic of Serbia, grant No. 6821-ATMOLCOL (B.P.M); US National Science Foundation No. PHY-2110318 (H.S.C).

- 
- [1] A. Saha, S. S. Nia, and J. A. Rodríguez, Electron diffraction of 3D molecular crystals, *Chem. Rev.* **122**, 13883 (2022).
- [2] K. Amini and J. Biegert, Chapter three – Ultrafast electron diffraction imaging of gas-phase molecules, *Adv. At. Mol. Opt. Phys.* **69**, 163 (2020).
- [3] B. P. Marinković, V. Vujčić, G. Sushko, D. Vudragović, D. P. Marinković, S. Dorjević, S. Ivanović, M. Nešvić, D. Jevremović, A. V. Solov'ov, and N. J. Mason, Development of collisional data base for elementary processes of electron scattering by atoms and molecules, *Nucl. Instr. Meth. Phys. Res. B* **354**, 90 (2015).
- [4] M. Dampc, A. R. Milosavljević, I. Linert, B. P. Marinković, and M. Zubek, Differential cross sections for low-energy elastic electron scattering from tetrahydrofuran in the angular range 20°-180°, *Phys. Rev. A* **75**, 042710 (2007).
- [5] A. Ponce, J. A. Aguilar, J. Tate, and M. J. Yacamán, Advances in the electron diffraction characterization of atomic clusters and nanoparticles, *Nanoscale Adv.* **3**, 311 (2021).
- [6] D. M. Kienzle and L. D. Marks, Surface transmission electron diffraction for SrTiO<sub>3</sub> surfaces, *Cryst. Eng. Comm.* **14**, 7833 (2012).
- [7] M. Gemmi, E. Mugnaioli, T. E. Gorelik, U. Kolb, L. Palatinus, P. Boullay, S. Hovmöller, and J. P. Abrahams, 3D electron diffraction: the nanocrystallography revolution, *ACS Central Sc.* **5**, 1315 (2019).
- [8] R. Aiswarya, R. Shaik, J. Jose, H. R. Varma, and H. S. Chakraborty, Simultaneous real and momentum space electron diffraction from a fullerene molecule, *Phys. Rev. Lett.* **133**, 033002 (2024).
- [9] E. G. Dymond, On electron scattering in helium, *Phys. Rev.* **29**, 433 (1927).
- [10] E. C. Bullard and H. S. W. Massey, The elastic scattering of slow electrons in argon, *Proced. Roy. Soc. A* **130**, 579 (1931).
- [11] T. Jahnke, V. Mergel, O. Jagutzki, A. Czasch, K. Ullmann, R. Ali, V. Frohne, T. Weber, L. P. Schmidt, S. Eckart, M. Schöffler, S. Schöffler, S. Voss, A. Landers, D. Fischer, M. Schulz, A. Dorn, L. Spielberger, R. Moshhammer, R. Olson, M. Prior, R. Dörner, J. Ullrich, C. L. Cocke, and H. Schmidt-Böcking, *High-resolution momentum imaging – from Stern's molecular beam method to the COLTRIMS reaction microscope*, in *Molecular Beams in Physics and Chemistry from Otto Stern's Pioneering Exploits to Present-Day Feats*, Ed. B. Friedrich and H. Schmidt-Böcking (Springer, 2021).
- [12] E. G. Champenois, N. H. List, M. Ware, P. H. B. M. Britton, X. Cheng, M. Centurion, J. P. Cryan, and R. F. et al., Femtosecond electronic and hydrogen structural dynamics in ammonia imaged with ultrafast electron diffraction, *Phys. Rev. Lett.* **131**, 143001 (2023).
- [13] Y. Lee, K. Y. Oang, D. Kim, and H. Ihee, A comparative review of time-resolved x-ray and electron scattering to probe structural dynamics, *Struct. Dyn.* **11**, 031301 (2024).
- [14] M. Dinger, Y. Park, and W. Y. Baek, Elastic and inelastic electron scattering cross sections of trichlorofluoromethane, *Phys. Rev. A* **111**, 022809 (2025).
- [15] C. J. Joachain, *Quantum Collision Theory* (North Holland publishing company, New York, 1975).
- [16] M. J. Seaton, Quantum defect theory, in *Molecular Applications of Quantum Defect Theory* (Routledge, 2019) p. 108.
- [17] N. F. Mott and I. N. Sneddon, *Wave Mechanics and Its Applications* (Oxford At the Clarendon Press, London, England, 1948).
- [18] N. F. Mott and H. S. W. Massey, *Theory of atomic collisions* (Oxford: Clarendon Press, London, England, 1933).
- [19] A. T. Stelbovics, Scattering theory of close-coupling equations, *Phys. Rev. A* **41**, 2536 (1990).
- [20] P. Descouvemont and D. Baye, The R-matrix theory, *Rep. Prog. Phys.* **73**, 036301 (2010).
- [21] T. Zuo, R. P. McEachran, and A. D. Stauffer, Relativistic distorted-wave calculation of electron impact excitation of xenon, *J. Phys. B: At. Mol. Opt. Phys.* **24**, 2853 (1991).
- [22] M. A. Khakoo, P. Vandeventer, J. G. Childers, I. Kanik, C. J. Fontes, K. Bartschat, V. Zeman, D. H. Madison, S. Saxena, R. Srivastava, and A. D. Stauffer, Electron impact excitation of the argon 3p<sup>5</sup>4s configuration: differential cross-sections and cross-section ratios, *J. Phys. B: At. Mol. Opt. Phys.* **37**, 247 (2003).
- [23] J. Čížek, On the correlation problem in atomic and molecular systems. Calculation of wavefunction components in Ursell-type expansion using quantum-field theoretical methods, *J. Chem. Phys.* **45**, 4256 (1966).
- [24] S. Bharti, L. Sharma, B. K. Sahoo, P. Malkar, and R. Srivastava, Application of relativistic coupled cluster theory to elastic scattering of electrons from confined Ca atoms, *J. Phys. B: At. Mol. Opt. Phys.* **52**, 185003 (2019).
- [25] F. Salvat, A. Jablonski, and C. J. Powell, ELSEPA—Dirac partial-wave calculation of elastic scattering of electrons and positrons by atoms, positive ions and molecules, *Comput. Phys. Commun.* **165**, 157 (2005).
- [26] B. Predojević, V. Pejčev, D. M. Filipović, D. Šević, and

- B. P. Marinković, Elastic electron scattering by a magnesium atom, *J. Phys. B: At. Mol. Opt. Phys.* **40**, 1853 (2007).
- [27] W. Williams and S. Trajmar, Electron impact excitation of magnesium at 10, 20 and 40 eV impact energies, *J. Phys. B: At. Mol. Opt. Phys.* **11**, 2021 (1978).
- [28] D. O. Brown, D. Cvejanović, and A. Crowe, The scattering of 40 eV electrons from magnesium: a polarization correlation study for the  $3^1P$  state and differential cross sections for elastic scattering and excitation of the  $3^1P$  and  $3^3P$  states, *J. Phys. B: At. Mol. Opt. Phys.* **36**, 3411 (2003).
- [29] S. Milisavljević, D. Šević, R. K. Chauhan, V. Pejčev, D. M. Filipović, R. Srivastava, and B. P. Marinković, Differential and integrated cross sections for the elastic electron scattering by calcium atom, *J. Phys. B: At. Mol. Opt. Phys.* **38**, 2371 (2005).
- [30] B. P. Marinković, R. P. McEachran, D. V. Fursa, I. Bray, H. Umer, F. Blanco, G. García, M. J. Brunger, L. Campbell, and D. B. Jones, Cross sections for electron scattering from cadmium: theory and experiment, *JPCRD* **52** (2023).
- [31] S. Jensen, D. Register, and S. Trajmar, Elastic and inelastic ( $5^1D$ ,  $6^1P$ ) electron scattering cross sections for barium, *J. Phys. B: At. Mol. Opt. Phys.* **11**, 2367 (1978).
- [32] S. Wang, S. Trajmar, and P. W. Zetner, Cross sections for electron scattering by ground state Ba: elastic scattering and excitation of the... $6s6p\ ^1P_1$  level, *J. Phys. B: At. Mol. Opt. Phys.* **27**, 1613 (1994).
- [33] J. H. Fregeau, Elastic and inelastic scattering of 187-MeV electrons from Carbon-12, *Phys. Rev.* **104**, 225 (1956).
- [34] B. R. Lewis, J. B. Furness, P. J. O. Teubner, and E. Weigold, The elastic scattering of electrons from argon, *J. Phys. B: At. Mol. Opt. Phys.* **7**, 1083 (1974).
- [35] J. C. Gibson, D. R. Lun, L. J. Allen, R. P. McEachran, L. A. Parcell, and S. J. Buckman, Low-energy electron scattering from xenon, *J. Phys. B: At. Mol. Opt. Phys.* **31**, 3949 (1998).
- [36] J. F. Williams and A. Crowe, The scattering of electrons from inert gases. II. Absolute differential elastic cross sections for neon, krypton and xenon atoms, *J. Phys. B: At. Mol. Opt. Phys.* **8**, 2233 (1975).
- [37] F. A. Gianturco and J. A. Rodriguez-Ruiz, Elastic scattering of low and intermediate-energy electrons by Kr and Xe atoms, *Zeitschr. Phys. D.* **31**, 149 (1994).
- [38] B. R. Lewis, I. E. McCarthy, P. J. O. Teubner, and E. Weigold, The elastic scattering of electrons from krypton, neon and xenon, *J. Phys. B: At. Mol. Opt. Phys.* **7**, 2549 (1974).
- [39] M. C. Cao, Y. Han, Z. Chen, Y. Jiang, K. X. Nguyen, E. Turgut, G. D. Fuchs, and D. A. Muller, Theory and practice of electron diffraction from single atoms and extended objects using an EMPAD, *Microscopy*, i150 (2018).
- [40] See Supplemental Material [url] for details of the methodology and numerical data of measurements which includes Refs. [17, 18, 25, 44–50].
- [41] S. Azizi, M. E. Madjet, Z. Li, J. M. Rost, and H. S. Chakraborty, Diffraction patterns in attosecond photoionization time delay, arXiv:2412.08204 [physics.atom-ph] (2024).
- [42] A. Rüdél, R. Hentges, U. Becker, H. S. Chakraborty, M. E. Madjet, and J. M. Rost, Imaging delocalized electron clouds: Photoionization of  $C_{60}$  in fourier reciprocal space, *Phys. Rev. Lett.* **89**, 125503 (2002).
- [43] M. Magrakvelidze, D. M. Anstine, G. Dixit, M. E. Madjet, and H. S. Chakraborty, Attosecond structures from the molecular cavity in fullerene photoemission time delay, *Phys. Rev. A* **91**, 053407 (2015).
- [44] W. R. Johnson, *Atomic structure theory* (Springer-Verlag Berlin Heidelberg, New York, 2007).
- [45] M. E. Rose and W. G. Holladay, *Relativistic Electron Theory* (Wiley, New York, 1961).
- [46] J. B. Furness and I. E. McCarthy, Semiphenomenological optical model for electron scattering on atoms, *J. Phys. B: At. Mol. Opt. Phys.* **6**, 2280 (1973).
- [47] D. R. Lide, *CRC handbook of chemistry and physics*, Vol. 85 (CRC press, Boca Raton, Florida, 2004).
- [48] F. Salvat, Optical-model potential for electron and positron elastic scattering by atoms, *Phys. Rev. A* **68**, 012708 (2003).
- [49] J. P. Perdew and A. Zunger, Self-interaction correction to density-functional approximations for many-electron systems, *Phys. Rev. B* **23**, 5048 (1981).
- [50] F. Salvat, J. M. Fernández-Varea, and W. Williamson Jr, Accurate numerical solution of the radial Schrödinger and Dirac wave equations, *Comput. Phys. Commun.* **90**, 151 (1995).
- [51] M. Ismail Hossain, A. K. F. Haque, M. Atiqur, R. Patoary, M. A. Uddin, and A. K. Basak, Elastic scattering of electrons and positrons by atomic magnesium, *Euro. Phys. J D* **70**, 1 (2016).
- [52] A. N. Tripathi and A. K. Jain, Spin polarization and cross sections in elastic scattering of electrons from Yb, Rn, and Ra atoms, *Phys. Rev. A* **61**, 032713 (2000).
- [53] M. Adibzadeh and C. E. Theodosiou, Elastic electron scattering from Ba and Sr, *Phys. Rev. A* **70**, 052704 (2004).
- [54] A. H. Hussain, A. K. Yassir, and A. Fallhy, Differential and total cross-sections for elastic scattering of electrons by cadmium atoms, *JCREST* **8**, 213 (2022).
- [55] D. Filipović, B. P. Marinković, V. Pejčev, and L. Vušković, Electron-impact excitation of krypton at incident electron energy of 60 eV, *Fizika* **20**, 421 (1988).
- [56] B. P. Marinković, V. Pejčev, D. M. Filipović, D. Šević, S. Milisavljević, and B. Predojević, Electron collisions by metal atom vapours, *Radiat. Phys. Chem.* **76**, 455 (2007).
- [57] C. E. Kuyatt and J. A. Simpson, Electron monochromator design, *Rev. Sci. Instrum.* **38**, 103 (1967).
- [58] A. Chutjian, Electron-impact excitation of the low-lying electronic states of formaldehyde, *J. Chem. Phys.* **61**, 4279 (1974).
- [59] M. A. McCune, M. E. Madjet, and H. S. Chakraborty, Unique role of orbital angular momentum in subshell-resolved photoionization of  $C_{60}$ , *J. Phys. B: At. Mol. Opt. Phys.* **41**, 201003 (2008).
- [60] R. Aiswarya, R. Shaik, J. Jose, H. R. Varma, and H. S. Chakraborty, EWS time delay in low energy e- $C_{60}$  elastic scattering, *Atoms* **12**, 18 (2024).
- [61] For scattering from Ca, TCS (not shown) shows a broader resonance extending to higher energy range. As a result, the FFT trend is found to better align with effective potential obtained using resonant cross sections.
- [62] H. Daimon, T. Matsushita, F. Matsui, K. Hayashi, and Y. Wakabayashi, Recent advances in atomic resolution three-dimensional holography, *Adv. Phys.: X* **9**, 1 (2024).
- [63] S. Ji, C. Jun, Y. Chen, and D. Wang, Precise synthesis at the atomic scale, *Precis. Chem.* **1**, 199 (2023).

- [64] S. S. Harilal, M. C. Phillips, D. H. Froula, K. K. Anoop, R. C. Issac, and F. N. Beg, Optical diagnostics of laser-produced plasmas, *Rev. Mod. Phys.* **94**, 035002 (2022).
- [65] Y. Rosandi, H. M. Urbassek, M. L. Nietiadi, and R. Alfaridzi, Astrophysical study of dust collision using molecular dynamics method: an overview, *J. Phys.: Conf. Ser.* **2915**, 012006 (2024).
- [66] J. C. Williamson, M. Dantus, S. B. Kim, and A. H. Zewail, Ultrafast diffraction and molecular structure, *Chem. Phys. Lett.* **196**, 529 (1992).
- [67] M. Centurion, T. J. A. Wolf, and J. Yang, Ultrafast imaging of molecules with electron diffraction, *Annu. Rev. Phys. Chem.* **73**, 21 (2022).